Deformation and failure of semicrystalline polymers under dynamic tensile and biaxial impact loading

J.P. Torres [a,*], P.M. Frontini [a], M. Machado [b], Z. Major [b]

[a] *Institute of Materials Science and Technology (INTEMA), Universidad Nacional de Mar del Plata, J. B. Justo 4302, 7600 Mar del Plata, Argentina*
[b] *Institute of Polymer Product Engineering (IPPE), Johannes Kepler Universität Linz, Altenbergerstrasse 69, 4040 Linz, Austria*

ARTICLE INFO

ABSTRACT

We propose a constitutive model to aid in the engineering design of semicrystalline polymer components that may be subjected to biaxial impact loading. To this end, we investigate the thermomechanical and failure behaviour of high density polyethylene (HDPE) under dynamic loading, both experimentally and analytically. We have carried out dynamic tensile tests at 10^1, 10^2 and 10^3 mm/s displacement rates. Digital image correlation (DIC) and infrared thermography were used to measure full 2D true strain fields and determine specimen temperature rise during tensile testing. The results were used to calibrate the constitutive parameters. To analyse the biaxial impact response, we have carried out falling weight impact (FWI) tests at a 4 m/s impact velocity. We assessed the model prediction capabilities by comparing numerical predictions with experimental results and good agreement was observed. The proposed model, which aims to achieve a compromise between prediction accuracy and formulation simplicity, shows that initial linear elastic response coupled with a temperature-dependent power-law viscoplastic flow element and a non-linear strain-hardening element are sufficient to model biaxial stress scenarios.

© 2016 Elsevier Ltd. All rights reserved.

1. Introduction

HDPE is widely used in a variety of high impact strength demanding applications such as load-bearing biomedical implants [1], automotive fuel tanks [2], pipe protection for oil and gas transportation [3], industrial vessels and liquid food containers [4]. During service, these components may undergo accidental drop or crash loading. Thus, there is an industrial concern in predicting how these parts will perform under such impact conditions. The traditional approach when designing impact-energy absorbing components involves costly and time-consuming trial-and-error tests on actual prototypes [5]. A more recent strategy is the prediction of material response using computer-assisted finite element (FE) simulations [6]. This approach is more cost-efficient and several commercial FE codes are currently available. However, the complex non-linear elasto-viscoplastic behaviour of plastics introduces several difficulties in the experimental assessment and constitutive modelling of polymer response. Hence, these fields remain under continuous development.

A number tests are frequently used to determine the performance of polymers under impact conditions including Charpy, Izod and Falling Weight Impact (FWI). The instrumented FWI test is specifically used to measure the biaxial in-plane tensile impact resistance under out-of-plane loading conditions [7]. This test is of technological interest since it develops a stress state in the specimen which closely represents the conditions that arise when loading shell-like components such as those obtained by injection moulding, extrusion or blow moulding processes. However, to this day there are no well-established direct procedures to use FWI test results for determining material intrinsic behaviour quantitative structural design and prediction. Consequently, FWI testing is mostly used as a pass/fail test or to present comparative rankings of material impact resistance [8]. An interesting non-conventional application of the FWI is to use it for material model validation. That is, to assess how well a model can predict deformation of a material outside the conditions under which it was calibrated. An example of this approach are the investigations carried out by Duan et al. [9,10], Du Bois et al. [11], Polanco-Loria et al. [12] and Daiyan et al. [13].

Several investigations have dealt with the experimental determination of polymer phenomenological response. During tensile testing, instabilities and inhomogeneities may be developed as a result of the underlying yield properties of the material [14]. This poses difficulties in the measurement of point-wise strain: to obtain a correct determination of the intrinsic true stress–strain relation, strain must be measured on regions sufficiently small to approximate the local deformation as homogeneous. The work of G'Sell et al. [15–17] represented a major advance in the determination of thermoplastics intrinsic behaviour by the use of non-contact optical strain

---

* Corresponding author. Institute of Materials Science and Technology (INTEMA), Universidad Nacional de Mar del Plata, J. B. Justo 4302, 7600 Mar del Plata, Argentina. Fax: +542234810046.

E-mail address: jptorres@fi.mdp.edu.ar (J.P. Torres).

measuring techniques. At the present, inhomogeneous 3D strain fields can be measured with great accuracy by means of modern digital image correlation (DIC) techniques [18–20]. Another difficulty that may arise when testing at relatively high strain rates is material temperature increase due to heat induced by plastic deformation. Depending on specimen geometry and testing velocity the conditions can vary from isothermal to adiabatic. As a rule of thumb, in typical uniaxial testing, strain rates above 10^{-2} s^{-1} are considered to produce adiabatic heating conditions [14]. Therefore, when determining the intrinsic material response at high strain rates it is also necessary to carry out point-wise temperature measurements on the specimen [21].

Constitutive models developed for semicrystalline polymers range from phenomenological models, which typically fit true stress–strain curves using unidimensional equations [16,22], to tensor-based 3D micromechanistic and physically-inspired models. An example of the latter is the family of tridimensional models developed by several research groups [23–29] which have been refined over the years to capture several features of polymer deformation response including strain rate, temperature and pressure dependence, post-yield softening, orientation hardening and unloading and cyclic response. Nevertheless, The mathematical complexity of these models is significant and their implementation in FE codes is not straightforward [30]. Moreover, in some cases they require the non-trivial experimental determination of a large number of constitutive parameters. Relevant to the specific case of thermoplastic polymers under impact behavior is the work of Polanco et al. [12] who modelled the dynamic response of polypropylene in the three-point bending and plate impact tests using an advanced constitutive model of the aforementioned kind. Their predictions showed good agreement with experimental results. However, their study was not focused at the prediction of failure behavior.

The use of advanced constitutive models can also be coupled with failure models formulated on a continuum level [31]. This means that the microstructural features of the fracture process are omitted and are only accounted in an averaged sense, over a "smoothed" continuum element [32]. This approach has been recently considered as an alternative to more complex fracture mechanics formulations, especially in practical engineering analysis. Failure models of this kind often involve strain or stress based failure criteria and is more conveniently used together with FE analysis. A damage equation that is function of stress or strain tensor components is evaluated at each material element in the FE mesh. When the equation satisfies the failure condition, the element is considered as damaged and is either removed from the mesh or degraded.

Reasonably accurate results in the application of this technique to engineering polymers have been reported in Refs. [33–35].

Despite the numerous advances in polymer mechanics, its application to failure prediction of parts subjected to multiaxial impact loading conditions is still rare in the literature. Thus, the objective of the present investigation is the validation of a constitutive model for HDPE that aims to achieve a compromise between prediction accuracy and formulation simplicity. We analyse experimentally HDPE intrinsic stress–strain behaviour at moderately high strain rates (in the 10^{-1} to 10^{2} s^{-1} range) and we use these data for model calibration. Then, we assess the model prediction capabilities by contrasting simulations with experiments with the aim of validating this modelling approach as feasible predictive tool applicable in design.

2. Constitutive model

The constitutive model is based on the kinematic finite strain framework of previous models for thermoplastic polymers proposed by Bergström et al. [28,30]. The model consists of an arrangement of 3 separate elements: a linear elastic spring acts in series with a viscoplastic dashpot (network A), and a non-linear Langevin spring acts in parallel to both (network B). The linear spring represents the initial elastic response. The dashpot represents pressure and temperature dependent viscoplastic flow. The Langevin spring models the orientation hardening response at large deformations.

Fig. 1 shows a schematic rheological representation of the constitutive model. Since networks A and B act in parallel, the total Cauchy stress tensor $\mathbf{T}$ is given by:

$$\mathbf{T} = \mathbf{T}_A + \mathbf{T}_B \tag{1}$$

The deformation gradient $\mathbf{F} \equiv \partial \mathbf{x}/\partial \mathbf{X}$, which relates the position of a material point in the reference configuration, $\mathbf{X}$, to the current configuration, $\mathbf{x}$, is given by:

$$\mathbf{F} = \mathbf{F}_A = \mathbf{F}_B \tag{2}$$

In addition, the deformation gradient in network A, $\mathbf{F}_A$, may be multiplicatively decomposed into elastic and plastic components [36]:

$$\mathbf{F}_A = \mathbf{F}_A^e \mathbf{F}_A^p \tag{3}$$

where the relaxed configuration, $\mathbf{F}_A^p$, represents an intermediate state that is obtained by elastically unloading the material to a stress-free state.
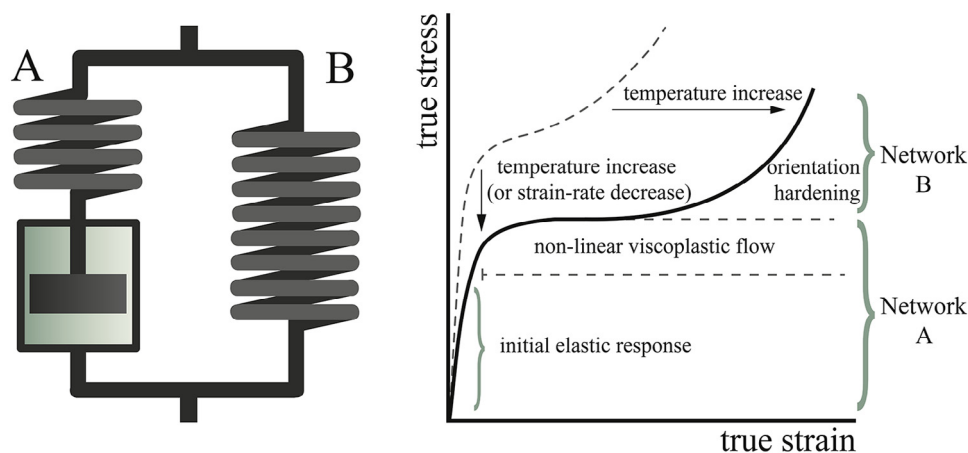
Fig. 1. 1D rheological representation of the constitutive model.

The total velocity gradient of network A, $\mathbf{L}_A = \dot{\mathbf{F}}_A \mathbf{F}_A^{-1}$, can be decomposed into elastic and plastic components: $\mathbf{L}_A = \mathbf{L}_A^e + \mathbf{F}_A^e \mathbf{L}_A^p \mathbf{F}_A^{e-1} = \mathbf{L}_A^e + \tilde{\mathbf{L}}_A^p$, where $\mathbf{L}_A^p = \dot{\mathbf{F}}_A^p \mathbf{F}_A^{p-1} = \mathbf{D}_A^p + \mathbf{W}_A^p$, and $\tilde{\mathbf{L}}_A^p = \tilde{\mathbf{D}}_A^p + \tilde{\mathbf{W}}_A^p$ is the velocity gradient in the current configuration. Following Ref. [28], it is convenient to prescribe $\tilde{\mathbf{W}}_A^p = 0$ to make the intermediate configuration unique (note that this definition causes the velocity gradient to be symmetric, $\tilde{\mathbf{L}}_A^p = \tilde{\mathbf{L}}_A^{pT}$).

The rate of shape change in network A, $\tilde{\mathbf{D}}_A^p$, is constitutively related to the driving stress by:

$$\tilde{\mathbf{D}}_A^p = \dot{\gamma}^p \frac{\mathbf{T}_A'}{\tau} \tag{4}$$

where $\mathbf{T}_A' = \text{dev}[\mathbf{T}_A]$ is the deviatoric part of the driving stress state on the relaxed configuration convected to the current configuration and $\tau = \sqrt{\text{tr}[\mathbf{T}_A' \mathbf{T}_A']/2}$ is the equivalent applied shear stress. These expressions allow to express the rate of the plastic deformation gradient as:

$$\dot{\mathbf{F}}_A^p = \dot{\gamma}^p \mathbf{F}_A^{e-1} \frac{\mathbf{T}_A'}{\tau} \mathbf{F} \tag{5}$$

It must be noted that a major simplification is introduced here by assuming plastic deformation to be related to the deviatoric stress only and, therefore, to take place at constant volume. We know from our experimental results that this is not the actual case (see Fig. 5 in Section 5). Despite this fact, we will assume that volumetric dilation effects can be neglected when predicting the macroscopical stress–strain response of an actual polymer component.

Equations (1)–(4) define the general kinematics. The material-specific behaviour is defined next by providing constitutive laws that relate the acting stresses, $\mathbf{T}_A$ and $\mathbf{T}_B$, with the deformation responses, $\mathbf{F}_A$ and $\mathbf{F}_B$.

The stress acting on network A is given by the linear elastic constitutive law:

$$\mathbf{T}_A = \frac{f_\theta^e}{J^e} \left(2\mu^e \mathbf{E}_A^e + \lambda^e \, \text{tr}[\mathbf{E}_A^e] \mathbf{I} \right) \tag{6}$$

Here $J^e = \det[\mathbf{F}^e]$, $\mathbf{E}_A^e = \ln[\mathbf{V}_A^e]$ is the logarithmic true strain or Hencky strain (where $\mathbf{V}_A^e = \sqrt{\mathbf{F}_A^e \mathbf{F}_A^{eT}}$), $\mathbf{I}$ is the second-order identity tensor, μ^e and λ^e are Lamé constants, the function f_θ^e models linear temperature dependence and is given by:

$$f_\theta^e(\theta) = \left[1 + q_\theta^e \left(\frac{\theta - \theta_0}{\theta_0} \right) \right] \tag{7}$$

where θ is the current temperature, θ_0 is the reference temperature and q_θ^e is the temperature scaling factor. The stress acting on the non linear strain-hardening spring on network B is given by the Arruda–Boyce eight-chain model [23]:

$$\mathbf{T}_B = \frac{\mu_h}{J \bar{\lambda}^*} \frac{\mathcal{L}^{-1}(\bar{\lambda}^*/\lambda_L)}{\mathcal{L}^{-1}(1/\lambda_L)} \text{dev}[\mathbf{B}^*] + \kappa(J-1)\mathbf{I} \tag{8}$$

μ_h is the hardening modulus, λ_L is the locking stretch, $\mathbf{B}^* = J^{-2/3} \mathbf{F} \mathbf{F}^T$ is the distortional part of the of the left Cauchy–Green tensor, $\bar{\lambda}^* = \sqrt{\text{tr}[\mathbf{B}^*]/3}$, $\mathcal{L}^{-1}(x)$ is the inverse Langevin function and κ is the bulk modulus. It must be noted that the eight-chain model was originally developed to represent entropic hyperelastic behaviour of rubbers and it has been also employed to model the hardening behaviour of glassy polymers [23]. For semicrystalline polymers the physical mechanisms producing molecular orientation hardening are radically different [37]. However, the stress–strain curves for semicrystalline polymers at large deformations closely resemble

Table A1
Constitutive parameters for the proposed model.

Property	Parameters	Value
Elastic	μ^e [MPa]	235
	λ^e [MPa]	1821
Viscoplastic	$\hat{\tau}$ [MPa]	9.81
	m	16.8
	f_f	1.9
	$\hat{\epsilon}$	0.014
Hardening	μ_h [MPa]	2.9
	λ_L	4.5
	κ [MPa]	2000
Pressure dependence	$\tau_{t/c}$	1
Temperature dependence	q_θ^e	−2.3
	q_θ^p	−0.36
Thermal	ω	0.6
	k [W/m.K]	0.49
	C_p [kJ/kg.K]	2.2
	θ_0 [K]	293

those of glassy polymers and, for that reason, we will employ the eight-chain model here.

Finally, we condensate all the phenomena resulting from plastic deformation in a power-law relationship that relates the plastic strain rate $\dot{\gamma}^p$ to the stress acting in the viscoplastic element:

$$\dot{\gamma}^p = \dot{\gamma}_0 \left(\frac{\tau}{f_{\epsilon^p} f_\theta^p f_p \tilde{\tau}} \right)^m \tag{9}$$

where $\hat{\tau}$ is the shear flow resistance, m is the shear flow exponent and $\dot{\gamma}_0 \equiv 1/s$ is a constant that is introduced to maintain dimensional consistency [38]. f_{ϵ^p} is a function that captures the initial non-linear yielding response:

$$f_{\epsilon^p} = f_f + (1 - f_f) \exp\left[\frac{-\epsilon_{vm}^p}{\hat{\epsilon}} \right] \tag{10}$$

where $\epsilon_{vm}^p = \sqrt{2/9 \left[(\epsilon_1^p - \epsilon_2^p)^2 + (\epsilon_2^p - \epsilon_3^p)^2 + (\epsilon_3^p - \epsilon_1^p)^2 \right]}$ is the applied effective Mises plastic strain, ϵ_i^p are the principal values of $\ln[\mathbf{B}^p]$, f_f is the final value of $\hat{\tau}$ after initial yielding and $\hat{\epsilon}$ is the characteristic transition strain. If the f_f parameter is >1, true stress increases after initial yielding, whereas $f_f < 1$ would represent softening after yielding. f_θ^p is a function that models the linear temperature dependence of the viscoplastic element according to:

$$f_\theta^p(\theta) = \left[1 + q_\theta^p \left(\frac{\theta - \theta_0}{\theta_0} \right) \right] \tag{11}$$

where θ, θ_0 and q_θ^p are defined in a similar fashion to equation (7). The use of power-law relationships to model the kinetic shear rate relation in semicrystalline polymers has been adopted previously in Refs. [24] and [28]. Finally, pressure dependence of the flow element is given by the function f_p:

$$f_p = r \tau_{t/c} + (1 - r) \tag{12}$$

where the parameter r is given by: $r = 0$, if $(\text{tr}[\mathbf{T}]/\sigma_{vm} \leq -1)$; $r = 1$, if $(\text{tr}[\mathbf{T}]/\sigma_{vm} \geq 1)$; or $r = \text{tr}[\mathbf{T}]/2\sigma_{vm} + 1/2$ otherwise. The thermomechanical parameters for the proposed constitutive model are presented in Table A1 and the parameter calibration procedure is described in Appendix A.

3. Experimental

The studied HDPE is a commercial grade HDPE 100. Samples for tensile and FWI tests we cut from extruded sheets of 2 mm nominal
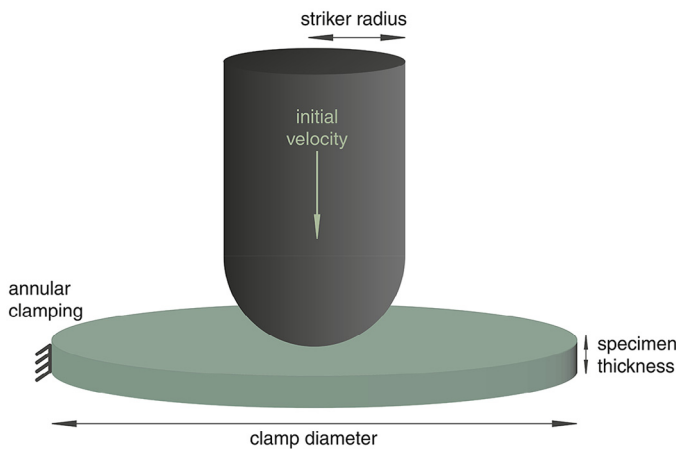
Fig. 2. Falling weight impact test geometry.

Fig. 3. Finite element mesh. (a) Tensile test. (b) FWI test.

thickness. To verify the repeatability of deformation and failure response, tests for each case and configuration were replicated 10 times. All tests were carried out at ambient temperature (20 °C).

3.1. Tensile tests

Dynamic tensile tests were performed on a MTS 852 servohydraulic damper test system using a 50 kN load cell. Tensile dog-bone specimens with ASTM D638 Type I geometry [39] were employed. Specimen gage section width and length are 10 mm and 130 mm respectively. High rate tests were performed at 10^1, 10^2 and 10^3 mm/s nominal displacement rate[1]. A SavitzkyGolay filter was applied to remove oscillations in the force signal introduced by the inertial effects of the testing aparatus. Local true strain measurements were obtained using a digital image correlation (DIC) technique with an ARAMIS system (GOM mbH). Temperature evolution of specimens during loading was remotely measured using a ThermoVision A 320G infrared camera produced by FLIR systems. The results of this testing combination are data sets containing local values for true stress, true longitudinal strain, true transverse strain, strain-rate and temperature.

3.2. Falling weight impact tests

Low-velociy FWI tests were carried out in an instrumented falling weight testing machine (Fractovis Ceast 6700) using a 23.7 kg striker mass and 4 m/s nominal impact velocity. In this test, a circular plate specimen is placed horizontally and clamped on its outer edges by an annular support of 40 mm diameter. Then, a vertically free-falling spherical striker with a 6.35 mm radius hits the specimen on its center (Fig. 2). A sensor measures the load on the striker and records it as a function of time. Molybdenum disulfide (Molikote®) lubricant was used on both the specimen and striker contact surfaces.

4. Finite element simulations

Simulations of the dynamic tensile and FWI tests were carried out in ABAQUS/Explicit 6.12 using a fully coupled thermal-stress dynamic analysis step which accounts for inertia effects, transient thermal response and temperature-dependent material response.
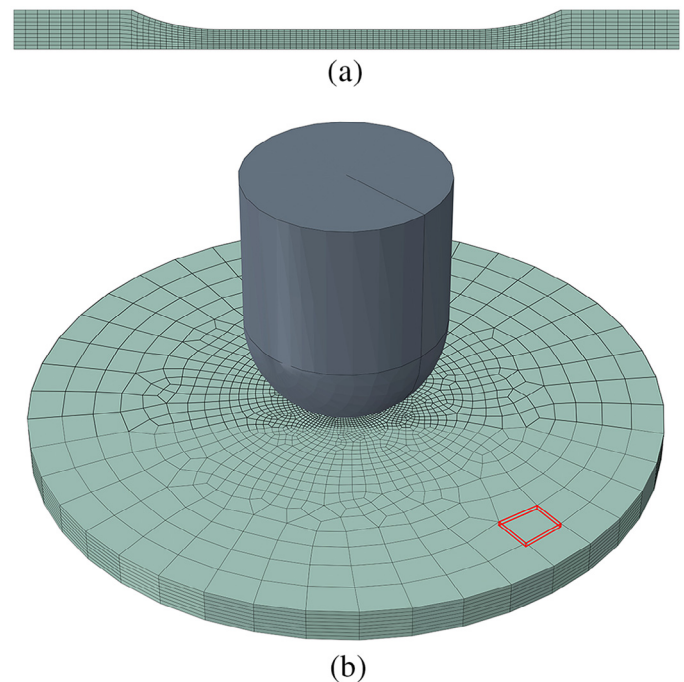
Temperature evolution is calculated in ABAQUS by performing the simultaneous integration of the momentum and heat transfer equations. This analysis allows to incorporate the inelastic energy dissipation as a heat source into the thermal energy balance and requires the specification of the material heat capacity C_p, thermal conductivity k and the inelastic heat fraction, ω, factor. The constitutive model is incorporated in ABAQUS as user material subroutine VUMAT using the commercial PolyUMod® library [38]. An initial uniform temperature of 20 °C was set in the entire geometry for both cases.

4.1. Tensile test

The tensile specimen was modelled using 4640 C3D8RT, 8-node continuum tridimensional hexahedral thermal-coupled, elements (Fig. 3a). Symmetry conditions were imposed in the thickness and width directions. The specimen gage and grip sections were modeled using 0.5 mm and 1.0 mm element sizes respectively. To mimic the loading of the grips, zero displacement boundary conditions were imposed on one end of the specimen, whereas a time-dependent displacement was imposed on the opposite end, using tabular displacement-time values from our experiments. These boundary conditions were applied to the entire volume of the grip section to better reproduce our experimental setting. A small imperfection consisting of a width reduction of 1% was introduced in order to induce necking. ALE (arbitrary Lagrangian–Eulerian) adaptive meshing option was used in order to enforce a constant mesh density in the neck where significant strain localization takes place.

4.2. Falling weight impact test

The FWI test was modelled using 10338 C3D8RT elements (Fig. 3b). Element size at the disc central region is 0.2 mm and is coarsened to 2 mm towards the edges. The striker was modelled as an analytical rigid surface. Clamping of the specimen was modelled enforcing zero-displacement of the nodes located along the specimen outer-edge. Surface-to-surface contact interaction between

---

[1] In this work, we use the term *nominal displacement rate* to refer to the crosshead rate set in the loading machine, which is different to the *true displacement rate* since the latter is not constant, i.e. it is affected by the inertial effects of acceleration from an initial zero velocity state.
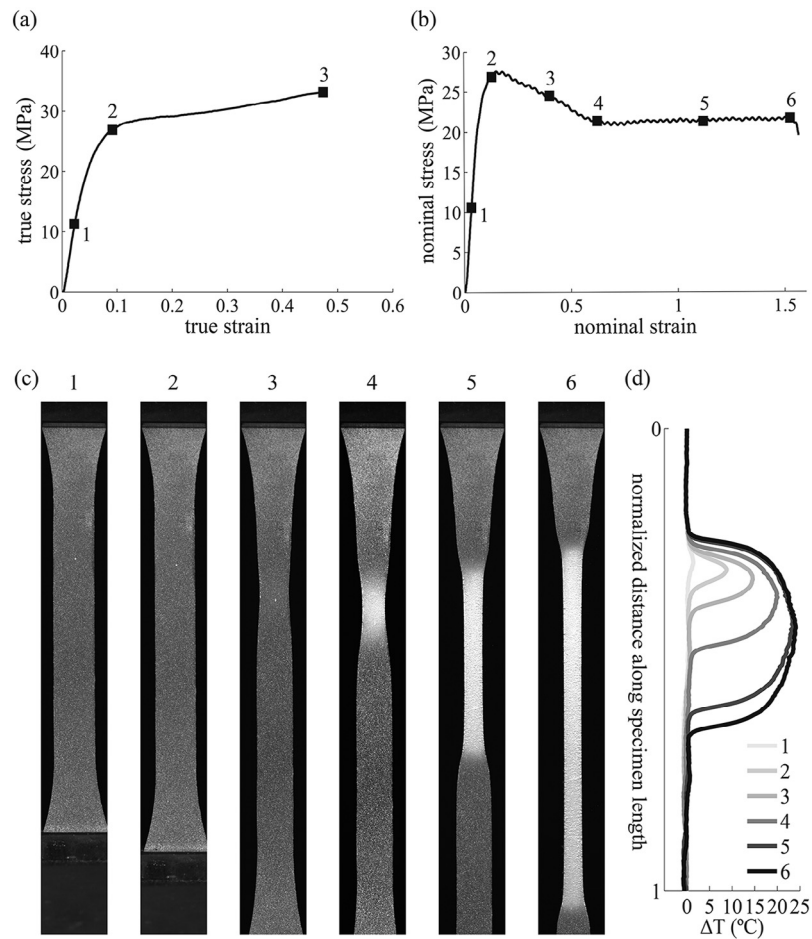
Fig. 4. Thermo-mechanical behaviour of HDPE in dynamic uniaxial testing at 10^2 mm/s. (a) True stress–strain behaviour, the dashed line represents tendency after DIC pattern breaks; (b) nominal stress–strain behaviour; (c, d) DIC camera images and IR measured temperature profiles along specimen gage, at different deformation stages.

the striker and disc was defined using a penalty-based contact formulation setting frictionless tangential behavior and *Hard contact* normal behaviour options available in ABAQUS [40]. The initial striker velocity was set as a boundary condition. Heat transfer between the specimen and surrounding media (including the striker) was neglected. The *enhanced hourglass control* and *element distortion control* options available in ABAQUS were included in order to prevent simulation premature termination due to excessive element distortion. Material failure was modelled using the element deletion technique available in ABAQUS/Explicit. This technique is known to be mesh-sensitive and requires the use of an appropriately dense 3D mesh for predictions to be reasonably accurate [34].

5. Results and analysis

5.1. Dynamic tensile behaviour

The observed response of HDPE specimens tested at 10^1, 10^2 and 10^3 mm/s is summarized in Fig. 4. DIC strain measurements were valid up to ≈0.6 true strain (Fig. 4a). Deformation is macroscopically homogeneous in the initial linear elastic region (1). At this stage the response is mainly due to deformation of the amorphous phase through the mechanisms of interlamellar slip, interlamellar separation and stack rotation [41]. After reaching the yield point (2), the material undergoes non-linear plastic flow where plastic deformation within the crystalline regions of the material is dominant [42]. At (3) initiation of necking is visible. Lamellar fragmentation and

beginning of fibrillation take place at this point [43], which is followed by chain disentanglement at (4). Next, the material undergoes stable neck propagation (points (4–5–6)) and eventually fails. The temperature rise reaches a maximum value of $\Delta T \approx 25$ °C (Fig. 4d) which remains constant during propagation of the neck. The main features of material volumetric deformation can be observed in Fig. 5, which shows Poisson's ratio, v, measured from DIC data as the ratio of transverse strain to longitudinal true strain. Here, it can be seen that deformation is not volume preserving (i.e. $v \neq 0.5$). Failure in HDPE occurs before complete neck propagation.
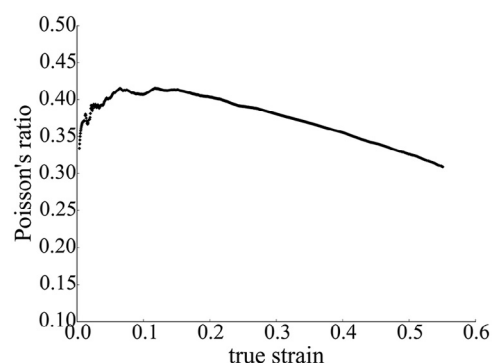

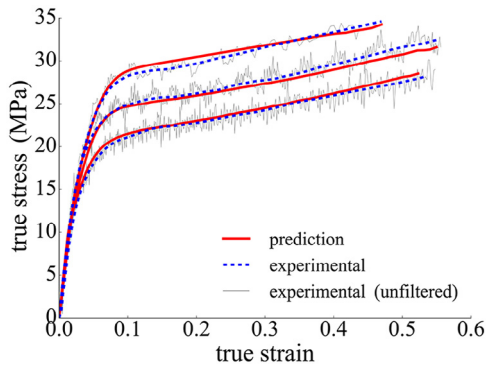**Fig. 5.** Poisson's ratio evolution during dynamic uniaxial testing of HDPE at 10^2 mm/s.

Fig. 6. Experimental vs. predicted stress–strain curves for HDPE under dynamic uniaxial tensile loading at 10^1, 10^2 and 10^3 mm/s.

Fig. 8. FEM predictions for HDPE temperature increase (ΔT) during dynamic uniaxial testing of HDPE at 10^2 mm/s. Each curve corresponds to deformation stages 1–6 shown in Fig. 4.

Tensile true stress–strain curves determined by DIC and the model predictions are shown in Fig. 6. The constitutive model shows good agreement with experimental curves. Fig. 7a shows the macroscopic force–displacement tensile curve for the test at a 10^2 mm/s displacement rate. Good agreement up to failure is observed. FE simulations of the tensile test predict the essential macroscopic features of the deformation response, i.e. initial homogeneous response and neck initiation followed by stabilization and propagation. FE predicted contour plots for the maximum principal logarithmic strain ϵ_I are also presented in Fig. 7b. Maximum ϵ_I value at failure is 1.289. The applicability of using this value to predict failure in biaxial
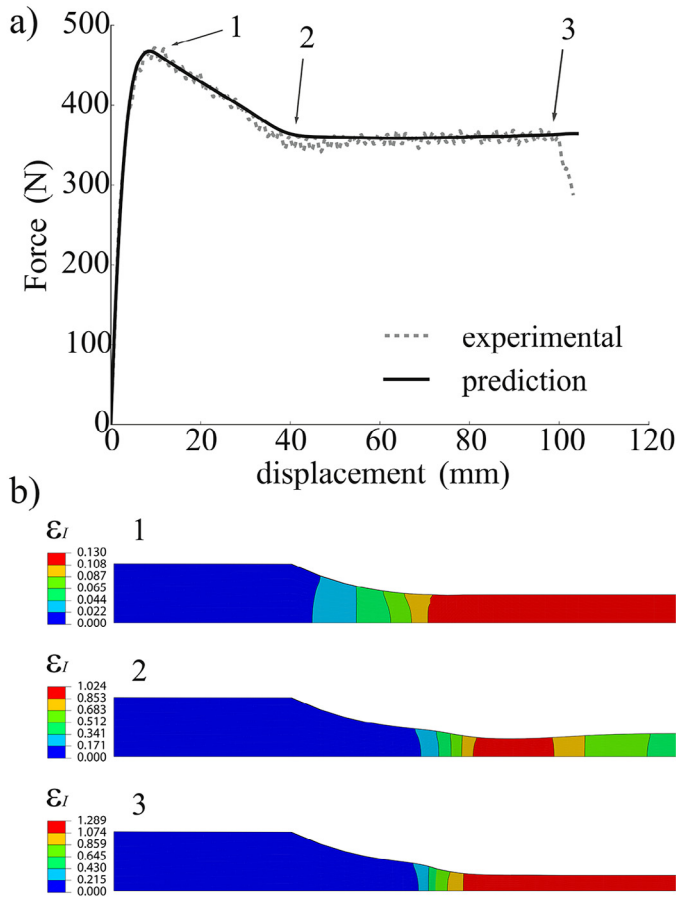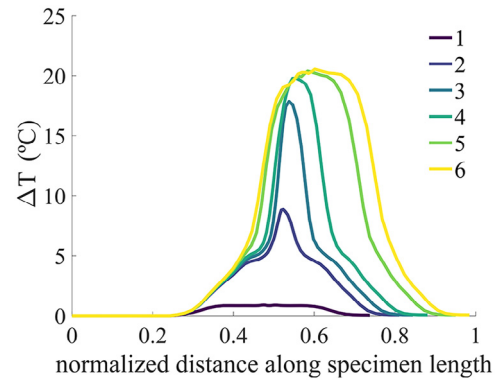

Fig. 7. Model predictions for HDPE dynamic tensile tests. (a) Experimental vs. predicted force–displacement curves. (b) Principal true strain ϵ_I contour plots at time points 1, 2 and 3, at 10^2 mm/s displacement rate.

impact will be addressed in the next section. Fig. 8 shows model predictions of the temperature increase (ΔT) along the specimen length for deformation stages 1–6 shown in Fig. 6. These curves can be compared to the experimental results (Fig. 6d). The maximum ΔT value and the general temperature distribution along specimen length are well approximated.

5.2. Falling weight impact behaviour

Fig. 9 presents simulation and experimental results for the FWI test at 4 m/s. In every case, specimen deformation presents drawing and thinning followed by ductile tearing failure (similar features were observed for HDPE in Ref. [44]). The dispersion in the t_f observed values is approximately 5%. Fig. 9a shows predicted and experimental F–t curves. Model predictions show good agreement with experimental results. Figs. 9b, 9c and 9d show ϵ_I contour plots at time points 1, 2 and 3 (indicated on Fig. 9a). Maximum values for temperature rise ΔT^{max} and strain rate $\dot{\epsilon}_{\text{max}}$ are also indicated and their location coincides with that of the maximum strain. In point 1, where the impact load is approximately 70% of the maximum, the material is beginning to yield. Here, $\dot{\epsilon} \approx 100\,\text{s}^{-1}$ in the central disc region, on the face opposite to the impact surface. Absorbed energy is 19% of the total impact energy. When the specimen receives the maximum impact load (point 2), $\epsilon_I \approx 0.8$ in the disc center and a circular region approximately equal to the striker diameter is undergoing plastic flow. At this point, 57% of the total impact energy has been absorbed. However, the material is still not experiencing significant orientation hardening. The strain rate has risen to $\dot{\epsilon} \approx 500\,\text{s}^{-1}$ and from this point on, it will start to decrease. At the failure point, t_F, the maximum principal strain reaches 1.327 in the disc center and orientation hardening has already taken place in a large portion of material under the striker tip.

A first attempt at modelling HDPE failure was also carried out. For this, we have employed the element-deletion technique (Section 4.2) using the ϵ_I value at failure observed in our simulations of the uniaxial tensile test at 10^2 mm/s: $\epsilon_I = 1.289$. Fig. 10b shows experimental and predicted fracture patterns of the FWI specimens. Key features such as failure initiation in the disc center, propagation of multiple radial cracks and a permanent deformed cap base are well predicted. A video animation of the deformation and failure simulation is available and accompanies the electronic version of this manuscript paper (Fig. 11) and also show the predicted F–t curve. Fair agreement with the experimental results of the global F–t response is observed. Nevertheless, the information obtained in the present investigation is not sufficient to define a suitable failure criterion: a critical value for failure should be determined from experimental measurements and confirmed under different stress
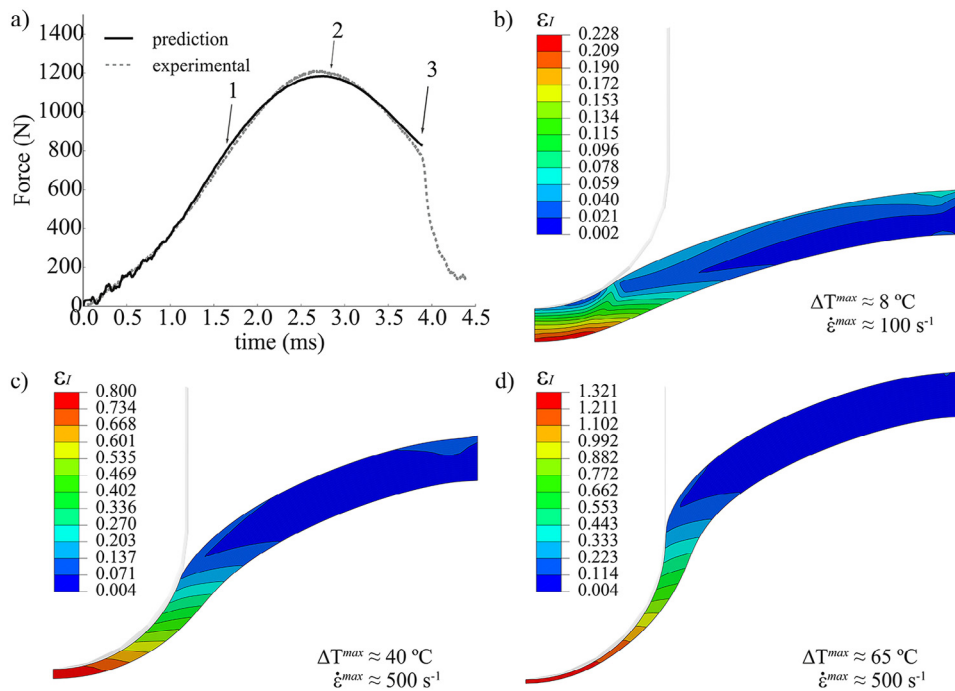
Fig. 9. FWI model predictions for HDPE at 4 m/s. (a) Experimental vs. predicted force–time curves. (b, c, and d) maximum principal true strain ϵ_I contour plots at the time points 1, 2 and 3 indicated in the F–t curve.

states. To achieve this, future investigations should employ an improved experimental protocol to measure deformation at larger strains. In addition, failure under different multiaxial stress states should also be experimentally assessed.

6. Conclusions

HDPE is among the most widely produced engineering polymers worldwide and are increasingly used in impact-resistance demanding applications. Biaxial impact scenarios are commonly encountered in accidental drop or crashing of shell, plate or hollow geometry components. However, rational predictive tools applicable in design of polymers to withstand impact loading situations have not yet been thoroughly established. In this paper, we proposed and validated a thermomechanical constitutive model that aims to achieve a compromise between prediction accuracy and formulation simplicity. Given the problem complexity, which includes non-homogeneous strain rate, temperature and deformation field distributions, the model is able to predict with fair accuracy the

experimental force–time curve of the falling weight impact test. Therefore, we show that initial linear elastic response, coupled with a temperature-dependent power-law viscoplastic flow element and a non-linear strain-hardening element are sufficient to model biaxial stress scenarios. In addition, we provide experimental infrared thermography data coupled with digital image correlation to understand temperature evolution during HDPE deformation at high velocity. A first attempt was made at modelling HDPE failure using an element deletion technique. Fracture patterns and force–time curve are well predicted. Nevertheless, the experimental information obtained in this investigation is not sufficient to accurately identify a failure criterion. Proposed future works include the validation of this model to other loading geometries and its extension to incorporate the effect of fillers such as rubber and/or mineral particles (typically added to increase toughness) on the impact response.

More accurate field predictions should also be obtained by incorporating strain rate dependence of the elastic response, temperature dependence of the orientation hardening element, volumetric component of plastic deformation and by refining the
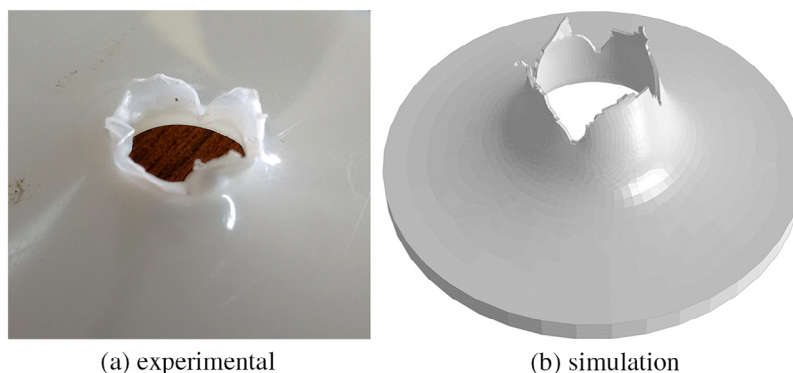

(a) experimental   (b) simulation

Fig. 10. Fracture aspect of HDPE specimens after impact testing: (a) tested specimen, (b) simulation.
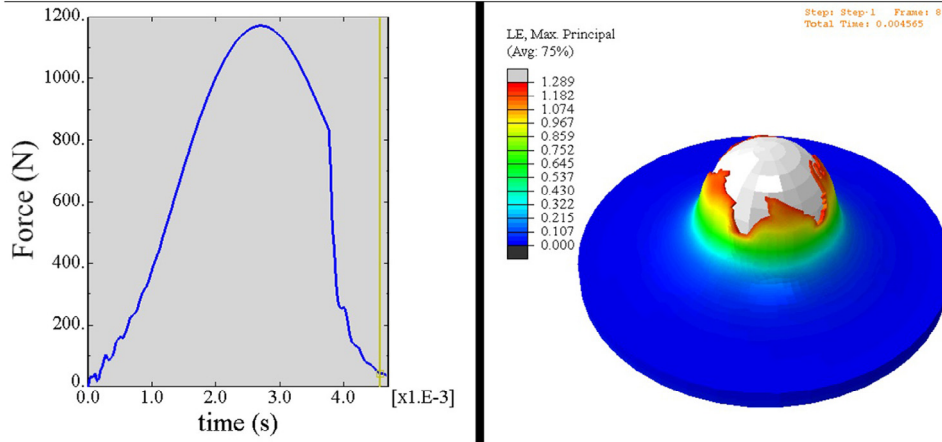
Fig. 11. Video animation of the FWI test simulation for HDPE including failure modelling.

parameter calibration procedure, especially the temperature and pressure dependence parameters.

Appendix A: Determination of constitutive parameters

The constitutive parameters were determined by an inverse method optimization procedure [45], which fits model simulations to the experimental stress–strain and force–displacement tensile curves, using the MCalibration® commercial software by Veryst Engineering. The calibration was carried out in a sequenced scheme as shown in Fig. A1: the elastic modulus was determined from the initial region of the stress–strain curve in the $0 < \epsilon < 0.05$ range (Fig. A1a). The initial shear flow resistance $\hat{\tau}$, the strain-rate dependence exponent m together with the evolution parameters for $\hat{\tau}$: f_f and $\hat{\epsilon}$ were determined in the $0.05 < \epsilon < 0.1$ range Fig. A1b. Following the orientation hardening parameters μ_h and λ_L and the temperature dependence parameter q_θ^p were determined from the stress–strain–temperature curves simultaneously in the $0.1 < \epsilon < 0.5$ region (Fig. A1c). A final fine-tuning optimization run was carried out calibrating all the parameters simultaneously using the complete stress–strain–temperature curves set together with the 1 m/s uniaxial force displacement (F–d) curve (Fig. A1d). The latter was necessary since our true strain DIC readings did not capture the entire deformation range. Poisson's ratio was determined using the DIC
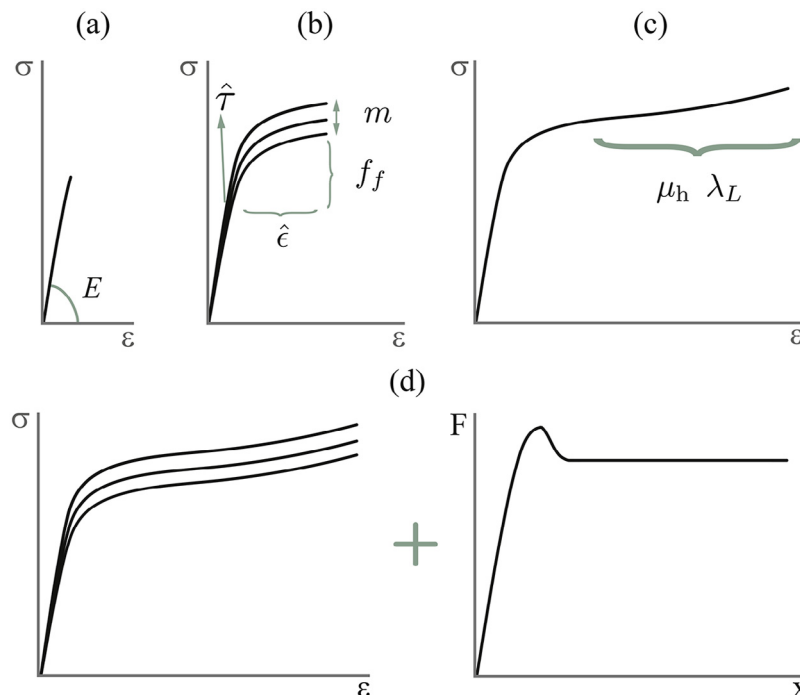

Fig. A1. Schematic representing parameter calibration procedure.

transverse strain data in the initial elastic region. Thermal properties k and C_p were taken from the manufacturer technical data sheet. The value for the inelastic heat fraction ω was approximated from values determined for polycarbonate in Ref. [46]. Seed values for the temperature dependence of yield stress were determined from the stress–temperature curves in Refs. [16] and [47] (after final inverse fitting they showed a significant decrease from their initial value). Values for the pressure dependency parameter $\tau_{t/c}$ were determined from data available in Refs. [48] and [49].

Appendix B: Thermodynamic consistency of the model

We demonstrate in this appendix that the proposed constitutive model is thermodynamically consistent. To this aim, we begin by considering the Clausius–Duhem inequality [50,51]:

$$\rho\dot{\psi} - \mathbf{T}:\mathbf{L} + \rho\eta\dot{\theta} + \frac{\mathbf{q}\cdot\nabla_{\mathbf{x}}(\theta)}{\theta} \leq 0$$

where ψ is Helmholtz free energy, η is the specific entropy, $\mathbf{q}$ is the heat flux vector, $\mathbf{T}$ is the Cauchy stress, $\nabla\mathbf{x}(\theta)$ is the temperature gradient, ρ is the density, θ is the absolute temperature and the symbol (:) denotes the tensor inner product ($\mathbf{A}:\mathbf{B} = A_{ij}B_{ij}$).

If we consider ψ, η, $\mathbf{T}$ and $\mathbf{q}$ to be dependent on the state variables $\{\mathbf{F}, \mathbf{F}_A^p, \nabla_{\mathbf{x}}(\theta), \theta\}$, the Clausius–Duhem inequality can be written as [52]:

$$\rho\left(\frac{\partial\psi}{\partial\mathbf{F}}\right):\dot{\mathbf{F}} + \rho\left(\frac{\partial\psi}{\partial\theta}\right)\dot{\theta} + \rho\left(\frac{\partial\psi}{\partial\nabla_{\mathbf{x}}(\theta)}\right):\dot{\nabla}_{\mathbf{x}}(\theta)$$
$$+ \rho\left(\frac{\partial\psi}{\partial\mathbf{F_A^p}}\right):\dot{\mathbf{F}}_A^p - \mathbf{T}:\mathbf{L} + \rho\eta\dot{\theta} + \frac{\mathbf{q}\cdot\nabla_{\mathbf{x}}(\theta)}{\theta} \leq 0 \tag{B.1}$$

Since this must hold for any process, $\eta = -\partial_\theta\psi$ and $\partial_{\nabla_{\mathbf{x}}(\theta)}\psi = 0$. We can also express the stress in terms of the strain energy density, W, as:

$$\mathbf{T} = \frac{1}{J}\frac{\partial W(\mathbf{F}, \theta, \mathbf{F}_A^p)}{\partial\mathbf{F}}\mathbf{F}^T$$

And therefore, $\mathbf{T}:\mathbf{L} = \dfrac{1}{J}\dfrac{\partial W(\mathbf{F}, \theta, \mathbf{F}_A^p)}{\partial\mathbf{F}}:\dot{\mathbf{F}}$. Replacing these terms in Eq. (13) we obtain:

$$\rho\frac{\partial\psi}{\partial\mathbf{F}_A^p}:\dot{\mathbf{F}}_A^p + \frac{\mathbf{q}\cdot\nabla_{\mathbf{x}}(\theta)}{\theta} \leq 0$$

We can express the strain energy density in terms of the contributions from networks A and B:

$$\frac{1}{J}\frac{\partial W_A(\mathbf{F}, \theta, \mathbf{F}_A^p)}{\partial\mathbf{F}}\mathbf{F}^T + \frac{1}{J}\frac{\partial W_B(\mathbf{F}, \theta)}{\partial\mathbf{F}}\mathbf{F}^T = \mathbf{T}_A + \mathbf{T}_B$$

And therefore we can write an equivalent expression for $\mathbf{T}_A$ as:

$$\mathbf{T}_A = \frac{1}{J_A^e}\frac{\partial W_A(\mathbf{F}, \theta, \mathbf{F}_A^p)}{\partial\mathbf{F}_A^e}\mathbf{F}_A^{eT}$$

And then, $\rho\dfrac{\partial\psi}{\partial\mathbf{F}_A^p}:\dot{\mathbf{F}}_A^p = -\mathbf{T}_A:\tilde{\mathbf{L}}_A^p$, therefore the Clausius–Duhem inequality can be expressed as:

$$\mathbf{T}_A:\tilde{\mathbf{L}}_A^p - \frac{\mathbf{q}\cdot\nabla_{\mathbf{x}}(\theta)}{\theta} \geq 0$$

Now, from Eq. (4) we have that $\tilde{\mathbf{D}}_A^p = \tilde{\mathbf{L}}_A^p = \dot{\gamma}^p\dfrac{\text{dev}[\mathbf{T}_A]}{\tau}$, therefore:

$$\mathbf{T}_A:\tilde{\mathbf{L}}_A^p = \mathbf{T}_A:\dot{\gamma}^p\frac{\text{dev}[\mathbf{T}_A]}{\tau}$$

To analyse the sign of this expression we turn to Einstein's summation notation:

$$\mathbf{T}_A:\dot{\gamma}^p\frac{\text{dev}[\mathbf{T}_A]}{\tau} \equiv T_{Aij}\left(T_{Aij} - T_{Akk}\delta_{ij}\right)\frac{\dot{\gamma}^p}{\tau}$$
$$= \left(T_{Aij}T_{Aij} - T_{Akk}T_{Aij}\delta_{ij}\right)\frac{\dot{\gamma}^p}{\tau}$$
$$= \left(T_{Aij}T_{Aij} - T_{Akk}T_{Aii}\right)\frac{\dot{\gamma}^p}{\tau}$$
$$= \left(T_{Aij}T_{Aij} - T_{Akk}^2\right)\frac{\dot{\gamma}^p}{\tau}$$
$$= \left(2T_{A12}^2 + 2T_{A13}^2 + 2T_{A23}^2\right)\frac{\dot{\gamma}^p}{\tau}$$

which satisfies $\mathbf{T}_A:\tilde{\mathbf{L}}_A^p \geq 0$ since $\dot{\gamma}^p$ and τ are always positive. By taking $\mathbf{q} = -\mathbf{K}(\mathbf{F}, \theta)\nabla_{\mathbf{x}}(\theta)$ where $\mathbf{K}$ is a positive semi-definite heat conductivity tensor, the dissipation inequality is automatically satisfied for all thermomechanical processes.

Supplementary data

The following is the supplementary data to this article:

References

[1] Pruitt L, Furmanski J. Polymeric biomaterials for load-bearing medical devices. JOM 2009;61(9):14–20.
[2] High Density Polyethylene Product Safety Summary, ExxonMobil Chemical Report. <https://www.exxonmobilchemical.com/Chem-English/Files/Resources/hdpe-resins-product-safety-summary.pdf>; 2015.
[3] Rueda F, Torres J, Machado M, Frontini P, Otegui J. External pressure induced buckling collapse of High Density Polyethylene (HDPE) liners: FEM modeling and predictions. Thin-Walled Struct 2015;96:56–63.
[4] Product Safety Assessment: High Density Polyethylene (HDPE) Resins, 2014, The Dow Chemical Company report ID No. 233-00577-MM-0214X.
[5] Campo EA. Selection of polymeric materials: how to select design properties from different standards. Norwich, NY: William Andrew; 2008.
[6] Bathe K-J. Res.2-002 finite element procedures for solids and structures, Massachusetts Institute of Technology: MIT OpenCourseWare. <http://ocw.mit.edu>; spring 2010 [accessed 23.12.15].
[7] ISO. 6603-2. 2000, Plastics – Determination of puncture impact behaviour of rigid plastics – Part 2: Instrumented impact testing. Geneva, Switzerland: International Organization for Standardization; 2000.
[8] Lampman S. Characterization and Failure Analysis of Plastics. Materials Park: ASM International; 2003.
[9] Duan Y, Saigal A, Greif R, Zimmerman M. Analysis of multiaxial impact behavior of polymers. Polym Eng Sci 2002;42(2):395–402.
[10] Duan Y, Saigal A, Greif R, Zimmerman M. Impact behavior and modeling of engineering polymers. Polym Eng Sci 2003;43(1):112.
[11] Du Bois P, Kolling S, Koesters M, Frank T. Material behaviour of polymers under impact loading. Int J Impact Eng 2006;32(5):725–40.
[12] Polanco-Loria M, Clausen AH, Berstad T, Hopperstad OS. Constitutive model for thermoplastics with structural applications. Int J Impact Eng 2010;37(12):1207–19.
[13] Daiyan H, Grytten F, Andreassen E, Osnes H, Lyngstad O. Numerical simulation of low-velocity impact loading of a ductile polymer material. Mater Des 2012;42:450–8.
[14] Ward IM, Sweeney J. Mechanical Properties of Solid Polymers. Chichester: John Wiley & Sons; 2012.
[15] Sell CG, Bai S-L, Hiver J-M. Polypropylene/polyamide 6/polyethylene–octene elastomer blends. part 2: volume dilatation during plastic deformation under uniaxial tension. Polymer (Guildf) 2004;45(17):5785–92.
[16] G'sell C, Jonas J. Determination of the plastic behaviour of solid polymers at constant true strain rate. J Mater Sci 1979;14(3):583–91.
[17] Duffo P, Monasse B, Haudin J, G'sell C, Dahoun A. Rheology of polypropylene in the solid state. J Mater Sci 1995;30(3):701–11.
[18] Balieu R, Lauro F, Bennani B, Haugou G, Chaari F, Matsumoto T, et al. Damage at high strain rates in semi-crystalline polymers. Int J Impact Eng 2015;76:1–8.
[19] Jerabek M, Major Z, Lang R. Strain determination of polymeric materials using digital image correlation. Polym Test 2010;29(3):407–16.

[20] Grytten F, Daiyan H, Polanco-Loria M, Dumoulin S. Use of digital image correlation to measure large-strain tensile properties of ductile thermoplastics. Polym Test 2009;28(6):653–60.

[21] Pawlak A, Rozanski A, Galeski A. Thermovision studies of plastic deformation and cavitation in polypropylene. Mech Mater 2013;67:104–18.

[22] Duan Y, Saigal A, Greif R, Zimmerman M. A uniform phenomenological constitutive model for glassy and semicrystalline polymers. Polym Eng Sci 2001;41(8):1322–8.

[23] Arruda EM, Boyce MC, Jayachandran R. Effects of strain rate, temperature and thermomechanical coupling on the finite strain deformation of glassy polymers. Mech Mater 1995;19(23):193–212. <http://dx.doi.org/10.1016/0167-6636(94)00034-E>.

[24] Lee B, Argon A, Parks D, Ahzi S, Bartczak Z. Simulation of large strain plastic deformation and texture evolution in high density polyethylene. Polymer (Guildf) 1993;34(17):3555–75.

[25] van Dommelen J, Parks D, Boyce M, Brekelmans W, Baaijens F. Micromechanical modeling of the elasto-viscoplastic behavior of semi-crystalline polymers. J Mech Phys Solids 2003;51(3):519–41.

[26] Ahzi S, Makradi A, Gregory R, Edie D. Modeling of deformation behavior and strain-induced crystallization in poly (ethylene terephthalate) above the glass transition temperature. Mech Mater 2003;35(12):1139–48.

[27] Ayoub G, Zari F, Nat-Abdelaziz M, Gloaguen J. Modelling large deformation behaviour under loading–unloading of semicrystalline polymers: application to a high density polyethylene. Int J Plasticity 2010;26(3):329–47.

[28] Bergström JS, Bischoff JE. An advanced thermomechanical constitutive model for UHMWPE. Int J Struct Changes Solids 2010;2(1):31–9.

[29] Pouriayevali H, Arabnejad S, Guo Y, Shim V. A constitutive description of the rate-sensitive response of semi-crystalline polymers. Int J Impact Eng 2013;62:35–47.

[30] Bergström J. Mechanics of solid polymers. San Diego: Elsevier; 2012.

[31] Krajcinovic D. Damage mechanics. Mech Mater 1989;8(2):117–97.

[32] Gearing BP. Constitutive equations and failure criteria for amorphous polymeric solids [Ph.D. thesis]. Massachusetts Institute of Technology; 2002.

[33] Bergström J, Rimnac C, Kurtz S. Molecular chain stretch is a multiaxial failure criterion for conventional and highly crosslinked UHMWPE. J Orthop Res 2005;23(2):367–75, <http://dx.doi.org/10.1016/j.orthres.2004.08.014>.

[34] Gearing B, Anand L. Notch-sensitive fracture of polycarbonate. Int J Solids Struct 2004;41(3):827–45.

[35] Torres J, Frontini P. Mechanics of polycarbonate in biaxial impact loading. Int J Solids Struct 2016;85:125–33.

[36] Lee EH. Elastic-plastic deformation at finite strains. J Appl Mech 1969;36(1):1–6.

[37] Argon A, Cohen R. Toughenability of polymers. Polymer (Guildf) 2003;44(19):6013–32.

[38] Bergström J. PolyUMod – A Library of Advanced User Materials, Veryst Engineering. Needham, Mass, USA: LLC; 2003.

[39] ASTM. D638 - 03. Standard Test Method for Tensile Properties of Plastics. West Conshohocken: ASTM International; 2003.

[40] Hibbit H, Karlsson B, Sorensen E. Abaqus User Manual, version 6.12. Providence, RI: Simulia; 2012.

[41] Galeski A. Strength and toughness of crystalline polymer systems. Prog Polym Sci 2003;28(12):1643–99.

[42] Redakcji O, Pawlak A, Galeski A. Cavitation during tensile drawing of semicrystalline polymers. Polimery 2011;56(9):627–36.

[43] Hiss R, Hobeika S, Lynn C, Strobl G. Network stretching, slip processes, and fragmentation of crystallites during uniaxial drawing of polyethylene and related copolymers. A comparative study. Macromolecules 1999;32(13):4390–403.

[44] Mohagheghian I, McShane G, Stronge W. Impact perforation of monolithic polyethylene plates: projectile nose shape dependence. Int J Impact Eng 2015;80:162–76.

[45] Polanco-Loria M, Daiyan H, Grytten F. Material parameters identification: an inverse modeling methodology applicable for thermoplastic materials. Polym Eng Sci 2012;52(2):438–48.

[46] Bouvard J, Francis D, Tschopp M, Marin E, Bammann D, Horstemeyer M. An internal state variable material model for predicting the time, thermomechanical, and stress state dependence of amorphous glassy polymers under large deformation. Int J Plasticity 2013;42:168–93. <http://dx.doi.org/10.1016/j.ijplas.2012.10.005>.

[47] Merah N, Saghir F, Khan Z, Bazoune A. Effect of temperature on tensile properties of hdpe pipe material. Plastics Rubber Composites 2006;35(5):226–30.

[48] Spitzig W, Richmond O. Effect of hydrostatic pressure on the deformation behavior of polyethylene and polycarbonate in tension and in compression. Polym Eng Sci 1979;19(16):1129–39.

[49] Mears D, Pae K, Sauer J. Effects of hydrostatic pressure on the mechanical behavior of polyethylene and polypropylene. J Appl Phys 1969;40(11):4229–37.

[50] Negahban M. The Mechanical and Thermodynamical Theory of Plasticity. Hoboken: CRC Press; 2012.

[51] Gurtin ME, Fried E, Anand L. The Mechanics and Thermodynamics of Continua. New York: Cambridge University Press; 2010.

[52] Bergström JS. Large strain time-dependent behavior of elastomeric materials [Ph.D. thesis]. Massachusetts Institute of Technology; 1999.